Electronic Supplementary Material (ESI) for Energy & Environmental Science.

Electronic Supplementary Information

Flexible three-dimensional interconnected piezoelectric ceramic foam based composites for highly efficient concurrent mechanical and thermal energy harvesting

Guangzu Zhang,‡[a,b] Peng Zhao,‡[c] Xiaoshan Zhang,[b] Kuo Han,[b] Tiankai Zhao,[c] Yong Zhang,[b] Chang Kyu Jeong,[b,d] Shenglin Jiang,[a] Sulin Zhang*[c] and Qing Wang*[b]

[a]School of Optical and Electronic Information, Huazhong University of Science and Technology, Wuhan, Hubei 430074, P. R. China

[b]Department of Materials Science and Engineering, The Pennsylvania State University, University Park, Pennsylvania, 16802, USA. E-mail: wang@matse.psu.edu

[c]Department of Engineering Science and Mechanics, The Pennsylvania State University, University Park, Pennsylvania, 16802, USA. E-mail: suz10@engr.psu.edu

[d]Division of Advanced Materials Engineering, Chonbuk National University, Jeonju, Jeonbuk 54896, Republic of Korea

‡These authors contributed equally to this work.

Note S1. Finite element modeling (FEM) of the piezoelectric active structures

In this section, a finite element technique for modeling the piezo-integrated composites is presented. A heterogeneous structure made out of polymer and piezoelectric materials (PZT) is considered without any geometrical restriction. Only elastic and piezoelectric effects are taken into account, and the model excludes nonlinearities as well as dissipative effects. The equations are developed in the case of a piezoelectric material. The case of an elastic material can be deduced by withdrawing physical variables and constants associated to electrical effects. Under these conditions, there are four equivalent representations commonly employed in the stationary theory of linear piezoelectricity to describe the coupled interaction between the electric and elastic variables. Here, the elastic strain ε_{ij}, and electric field E_i, are taken as the independent variables and are related to the stress σ_{ij} and the electric displacement D_i, by:

$$\sigma_{ij} = C_{ijmn}\varepsilon_{mn} - e_{nij}E_n \tag{1}$$

$$D_i = e_{imn}\varepsilon_{mn} - \epsilon_{in}E_n \tag{2}$$

where C_{ijmn}, C_{ijmn}, e_{nij} and ϵ_{in} are the elastic moduli (measured in a constant electric field), the piezoelectric coefficients (measured at a constant strain or electric field) and the dielectric constants (measured at a constant strain), respectively, with i, j, k and l varying from 1 to 3 and being related to the coordinate axis. Einstein notation is systematically used throughout the text. In equations (1) and (2), the strain and electric field are derivable from the elastic displacement and electric potential as:

$$\varepsilon_{ij} = \frac{1}{2}\left(u_{i,j} + u_{j,i}\right) \tag{3}$$

$$E_i = -\varphi_{,i} \tag{4}$$

where u denotes the displacement field, φ is the electric potential and a comma denotes partial differentiation.

Due to the crystal symmetries, the piezoelectric coupling matrix $[d]$ may have only few non-zero elements.

To complete the formulation of the stationary theory of piezoelectricity, equations (1)-(4) must be supplemented with the equations of elastic equilibrium and Gauss's law of electrostatics with in absence of any body forces and free charge:

$$\sigma_{ij,j} = 0 \tag{5}$$

$$D_{i,i} = 0 \tag{6}$$

Unless otherwise told, the conventional indicial notation is utilized where repeated subscripts are summed over the range 1-3. Generally, D_i and E_i are vectors, that is, Cartesian tensors of rank 1, and permittivity ϵ is a Cartesian tensor of rank 2. Strain and stress are, in principle, also rank-2 tensors. But conventionally, because the strain and stress are all symmetric tensors, with a poling direction denoted by 3. Equations (1) and (2) can also be represented as:

$$\begin{Bmatrix} \sigma_{11} \\ \sigma_{22} \\ \sigma_{33} \\ \sigma_{23} \\ \sigma_{31} \\ \sigma_{12} \end{Bmatrix} = \begin{bmatrix} c_{11} & c_{12} & c_{13} & 0 & 0 & 0 \\ c_{12} & c_{11} & c_{13} & 0 & 0 & 0 \\ c_{13} & c_{13} & c_{33} & 0 & 0 & 0 \\ 0 & 0 & 0 & c_{44} & 0 & 0 \\ 0 & 0 & 0 & 0 & c_{44} & 0 \\ 0 & 0 & 0 & 0 & 0 & c_{66} \end{bmatrix} \begin{Bmatrix} \varepsilon_{11} \\ \varepsilon_{22} \\ \varepsilon_{33} \\ 2\varepsilon_{23} \\ 2\varepsilon_{31} \\ 2\varepsilon_{12} \end{Bmatrix} - \begin{bmatrix} 0 & 0 & e_{31} \\ 0 & 0 & e_{31} \\ 0 & 0 & e_{33} \\ 0 & e_{15} & 0 \\ e_{15} & 0 & 0 \\ 0 & 0 & 0 \end{bmatrix} \begin{Bmatrix} E_1 \\ E_2 \\ E_3 \end{Bmatrix} \tag{7}$$

$$\begin{Bmatrix} D_1 \\ D_2 \\ D_3 \end{Bmatrix} = \begin{bmatrix} 0 & 0 & 0 & 0 & e_{15} & 0 \\ 0 & 0 & 0 & e_{15} & 0 & 0 \\ e_{31} & e_{31} & e_{33} & 0 & 0 & 0 \end{bmatrix} \begin{Bmatrix} \varepsilon_{11} \\ \varepsilon_{22} \\ \varepsilon_{33} \\ 2\varepsilon_{23} \\ 2\varepsilon_{31} \\ 2\varepsilon_{12} \end{Bmatrix} + \begin{bmatrix} \epsilon_{11} & 0 & 0 \\ 0 & \epsilon_{11} & 0 \\ 0 & 0 & \epsilon_{33} \end{bmatrix} \begin{Bmatrix} E_1 \\ E_2 \\ E_3 \end{Bmatrix} \quad (8)$$

Equations (7) and (8) are the most general representation of the constitutive behavior of piezoelectric materials.

The finite element (FE) model presented in the current study is developed on the basis that the complete coupled response of an infinitely large and periodically arranged second phase in the continuous matrix phase can be represented by characterizing the behavior of a much smaller three-dimensional representative volume element (cell). In particular, for the NP and NW composites, we only modeled a small representative cell out of the whole structure in an experimental length scale. To compare the simulated results with that of the relevant experiments, the electromechanical responses (i.e., voltage) are scaled with respect to the characteristic size of the cell. On the other hand, for the 3-3 type composite (with 3-D foam structured PZT inclusion), due to the characteristic size of the structure, the cell has the same size at the thickness direction as that in experimental samples. To model the 3D foam structure, we adopted the concept of the Weaire-Phelan structure, which is a complex 3-D structure representing an idealized foam of equal-sized bubbles. The Kelvin structure which is a better solution of simulations of foam structure is employed to represent the microstructure of PZT for the composites. A finalized structure, by periodically adjunct Kelvin cells together, is illustrated in ESI Fig. S1†.

Piezoelectric finite elements have been included in ABAQUS,[S1] one of the many commercially available finite element programs which have been widely used for FE modeling of piezoelectric media. When applying FE modeling to composite materials and structures, perfect bonding on the material interface is assumed. Thus, all the variables are continuous across the matrix-filler interface. Finite element method can be then employed to solve the equilibrium equations along with the boundary conditions. The fundamental elastic, piezoelectric and dielectric constants of each component are presented in ESI Table S1†.

Table S1. The fundamental electromechanical and thermal properties of the PZT and PDMS which are utilized to construct the composites.

	Mechanical			**Piezoelectric**					**Thermal**	
	Density (Kg/m^3)	*Young's modulus* (MPa)	*Poisson ratio*	d_{31}	d_{33}	d_{15}	$\varepsilon_{11}/\varepsilon_0$	$\varepsilon_{33}/\varepsilon_0$	*Conductivity* (W m^{-1} K^{-1})	*Specific heat* (J Kg^{-1} K^{-1})
				(×10^{-10} m/V)						
PZT	8000	60 000	0.31	-120	270	475	1250	1250	1.20	378
PDMS	1000	1	0.49	0	0	0	2.3	2.3	0.15	1350

To assess our multiphysical finite element model, piezoelectric responses of the composites with four different PZT fillers, i.e., randomly dispersed nanoparticles, randomly oriented nanowires, aligned nanowires, and 3-D foam composites have been studied. The NP and 3-D structures are generated by the random arrangement of the positions of fillers into the PDMS matrix, while the NW composites require the random arrangement of both the position and the orientation of the fillers. During this process, no intersections are allowed between fillers. The schematics of FE modeling using ABAQUS CAE are shown in ESI Fig S1†.

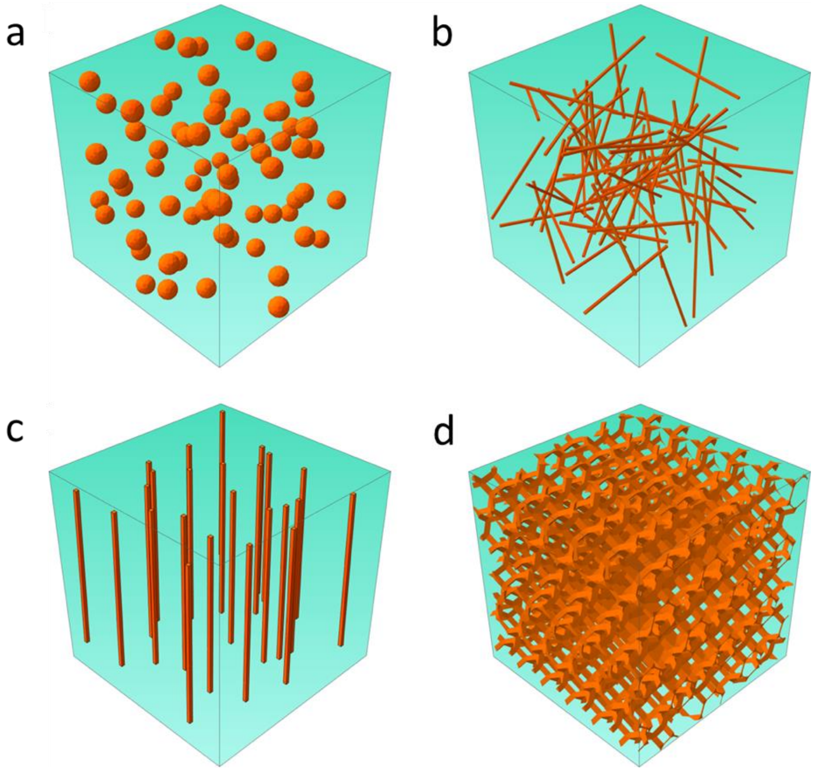

Fig. S1. Schematics of the finite element modeling for the composites with different types of fillers (PZT ceramics with various structures). (a) Randomly dispersed nanoparticles with an average diameter of 300 nm. (b) Randomly arranged NWs with a diameter of 100 nm and a length of 3 μm. (c) The composite with aligned NWs. (d) A bi-continuous nanocomposite with 3-D foam-like filler structure.

Note S2. Theoretical study on the load-transfer efficiency in the composites

To rationalize the superior piezoelectric performance of the 3-D composites, for the uniaxial compressing case, we estimated the load-transfer efficiency (LTE) within NP, NW and 3D foam structures, respectively. In this section, theoretical equations for the effective elastic, dielectric and piezoelectric constants for composites with NP, NW and 3D foam structures are obtained using the representative volume element (RVE) method.

Modeling of composites with spheroidal inclusions

Considering a two-phase system composed of a continuous matrix and spherical inclusions, one of the expressions for the effective dielectric constant is:[S2]

$$\epsilon_{33}^{*} = \epsilon_{33}^{\mathrm{PDMS}} \frac{\lambda+2+2\phi(\lambda-1)}{\lambda+2-\phi(\lambda-1)} \tag{9}$$

where $\lambda = \frac{\epsilon_{33}^{\mathrm{PZT}}}{\epsilon_{33}^{\mathrm{PDMS}}}$ is the ratio of dielectric constant of filler to the matrix. In the case of composites with PDMS matrix and PZT filler, $\lambda = 565.32 \gg 1$, thus

$$\epsilon_{33}^{*} = \epsilon_{33}^{\mathrm{PDMS}} \frac{1+2\phi}{1-\phi} \tag{10}$$

On the other hand, the elastic property is, in general, specified by two constants, i.e., bulk and shear moduli. Under the assumption that both phases are incompressible, we have

$$Y^{*} = Y^{\mathrm{PDMS}} \frac{2+3\kappa+3\phi(1-\kappa)}{2+3\kappa-2\phi(1-\kappa)} \tag{11}$$

where $\kappa = Y^{\mathrm{PDMS}}/Y^{\mathrm{PZT}}$ is the ratio of Young's modulus of the PDMS matrix to.PZT filler. Because the elastic constant of PZT is much larger than that of PDMS, that is $\kappa \approx 1/60000 \ll 1$, the effective Young's modulus can be estimated by:

$$Y^{*} = Y^{\mathrm{PDMS}} \frac{2+3\phi}{2-2\phi} \tag{12}$$

By making the assumption that piezoelectric constants of the PZT inclusion/nanoparticles are one-dimensional and relate the dielectric variable along one polar axis, the expressions for d_{33} can be explicitly written as:

$$d_{33}^{*} = d_{33}^{\mathrm{PZT}} \phi \varphi_T \varphi_E \tag{13}$$

where φ_T and φ_E are the local field coefficients of stress and electric, respectively.

$$\varphi_T = \frac{5}{2+3\kappa+3\phi(1-\kappa)} \tag{14}$$

$$\varphi_E = \frac{3}{\lambda+2-\phi(\lambda-1)} \tag{15}$$

Similarly, in the case that $\kappa \ll 1$ and $\lambda = 565.32 \gg 1$, the expressions for the effective d_{33} can be reduced to

$$d_{33}^{*} = d_{33}^{\mathrm{PZT}} \frac{5\phi}{2+3\phi} \frac{3}{\lambda+2-\phi(\lambda-1)} \tag{16}$$

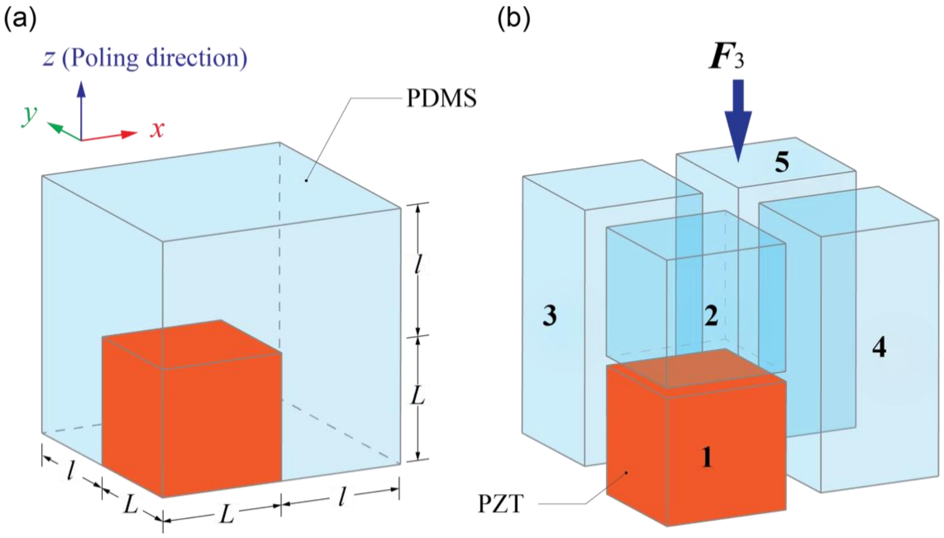

Fig. S2. Unit cell and force distribution in the NP composite. (a) Model of the interpenetrating structures of two components (piezoelectric and polymer phases) with volume fractions depending on the piezoelectric column width L and length l. (b) Force F_3 in z (poling) direction is distributed through volumes 1-5.

Now let us consider the LTE of the NP fillers. ESI Fig. S2† shows typical unit cell of composites with 0-3 connectivity (i.e., NP). If a force F_3 is applied onto the unit cell along the poling direction, the total force is distributed through five volumes as shown in ESI Fig. S2b†. Considering the whole structure is undergoing a strain ε_{33}, according to the structure shown in ESI Fig. S2b†, the effective strain on the PZT fillers can be written as:

$$\overline{\varepsilon_{33}^{\mathrm{PZT}}} = \frac{L+l}{L+l/\kappa}\varepsilon_{33} \tag{17}$$

In the case of $\kappa \ll 1$ and $L \sim l$, the LTE $\eta \equiv \varepsilon_{33}^{\mathrm{PZT}}/\varepsilon_{33}$ of PZT nanoparticles can be simplified as:

$$\eta_{\mathrm{NP}} = \frac{\kappa}{\left(1-\phi^{\frac{1}{3}}\right)} \tag{18}$$

where $\phi \equiv \frac{L^3}{(L+l)^3}$ denotes the volume fraction of PZT nanoparticle fillers. Let $\kappa = 1/60000$ and $\phi = 16\%$, $\eta_{\mathrm{NP}} = 3.6 \times 10^{-5}$.

Modeling of the composite with nanowires

Halpin-Tsai model[S3] describes the elastic properties of composites in terms of the elastic properties of the nanowires and the matrixes along with the nanowire orientations. Elastic moduli of composites with nanowires arranged longitudinal (Y_L) and transverse (Y_T) are given by:[S4]

$$Y_L = \frac{1+2\rho\zeta_L\phi}{1-\zeta_L\phi}Y^{\mathrm{PDMS}} \tag{19}$$

$$Y_T = \frac{1+2\zeta_T\phi}{1-\zeta_L\phi}Y^{\mathrm{PDMS}} \tag{20}$$

where

$$\zeta_L = \frac{1-\kappa}{1+2\kappa\rho_S} \tag{21}$$

$$\zeta_T = \frac{1-\kappa}{1+2\kappa} \tag{22}$$

and $\rho_S = \frac{l}{d}$ is the slenderness ratio of the nanowires. The elastic modulus of composites with random configurations can be written as:

$$Y_R = \frac{3}{8}Y_L + \frac{5}{8}Y_T \tag{23}$$

For the case where $\kappa \ll 1 \ll \rho_S$, $\eta_L = \eta_T = 1$, we have:

$$Y^* = Y_R = \frac{4+(3\rho+5)\phi}{4(1-\phi)} Y^{\mathrm{PDMS}} \tag{24}$$

The expressions for d_{33}^* can be explicitly written by multiplying that of PZT with the fraction of load experienced by the PZT:

$$d_{33}^* = d_{33}^{\mathrm{PZT}} \frac{(3\rho_S+1)\phi}{4+(3\rho_S+5)\phi} \tag{25}$$

Different from the isotropic NP composites, the LTE of NW based composites is strongly dependent on the orientation of the NWs relative to the loading direction. ESI Fig. S3† demonstrates the composite structures with NWs arranged longitudinal and transverse, respectively.

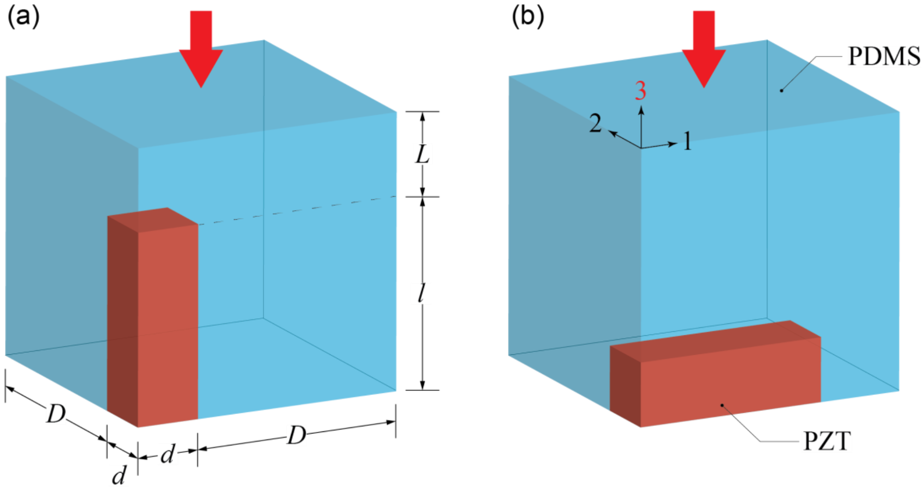

Fig. S3. Unit cell and the interpenetrating structures of two components (piezoelectric and polymer phases) with NWs arranged longitudinally and transversely ((a) and (b) respectively).

The LTE of the NW-based composites can be derived, for the longitudinal ($\eta_{\mathrm{NW,L}}$) and transverse ($\eta_{\mathrm{NW,T}}$) orientations, respectively:

$$\eta_{\mathrm{NW,L}} \simeq \frac{1+2\rho_S}{1-\phi} \kappa \tag{26}$$

$$\eta_{\mathrm{NW,T}} \simeq \frac{3}{1-\phi}\kappa \tag{27}$$

The LTE of the NW composites with random configurations can be written as:

$$\eta_{\mathrm{NW,R}} = \frac{3}{8}\eta_{\mathrm{NW,L}} + \frac{5}{8}\eta_{\mathrm{NW,T}} \tag{28}$$

With a volume fraction of PZT $\phi = 16\%$, slenderness ratio of nanowires $\rho_s = 30$ and $\kappa = 1/60000$, we have the effective LTE $\eta_{\mathrm{NW}} = 4.9 \times 10^{-4}$.

Modeling of 3-D foam composites

In the 3-D composites, the connectivity of both the components reaches a maximum, with both the components being continuously distributed in three dimensions. This high degree of connectivity favors high piezoelectric activity.

As the dielectric permittivity of the PZT is significantly greater than that of the polymer, ($\epsilon_{33}^{\mathrm{PZT}} \gg \epsilon_{33}^{\mathrm{PDMS}}$), it will dominate the effective permittivity ϵ_{33}^{*} of the composites. The effective dielectric permittivity of the composite can therefore be approximated by a formula[S5,S6]

$$\epsilon_{33}^{*} = \epsilon_{33}^{\mathrm{PZT}} \frac{1}{(1+\rho_A)^2} \tag{29}$$

where $\rho_A = \frac{l}{L}$ is the aspect ratio of the micro-foam structure as shown in ESI Fig. S4a†.

To calculate the effective piezoelectric coefficient d_{33}^{*}, a typical Banno unit cell for the 3-3 composites is adopted (shown in ESI Fig. S4a†), where the interpenetrating components are indicated. If a force F_3 is applied on the *z* direction, the total force is distributed through four volumes indicated in ESI Fig. S4b†. Because of its significantly higher compliance than the ceramics, the polymer component will experience less force, and has led to the assumption in some models of complete stress transfer into the piezoceramics.[S5]

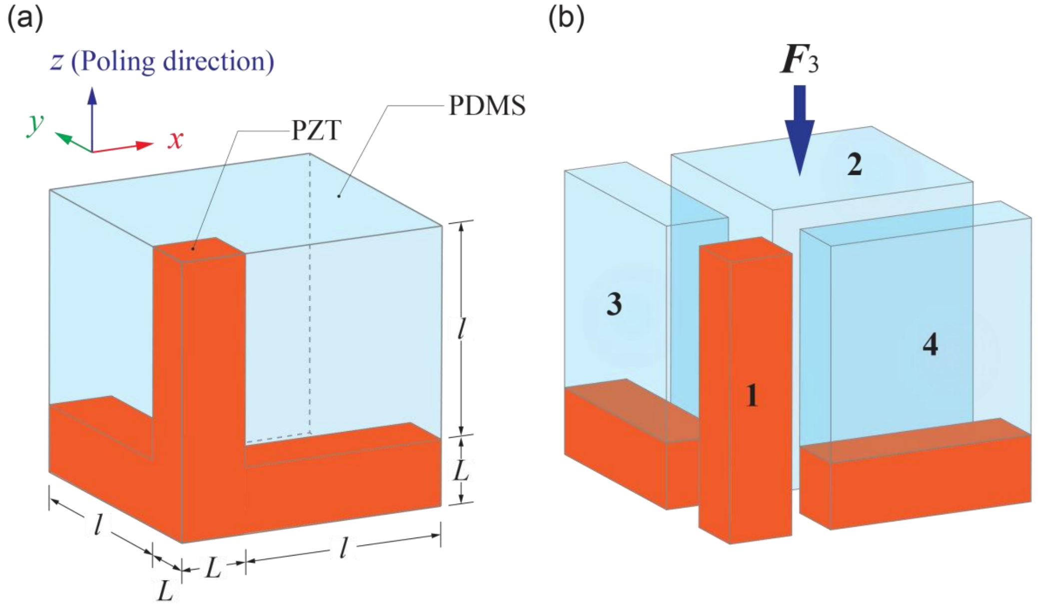

Fig. S4. The Banno unit cell and the distribution of forces in the 3-3 ceramic-polymer composites. (a) Model of the interpenetrating structures of two components (piezoelectric and polymer phases) with volume fractions depending on the piezoelectric column width L and length l. (b) Force F_3 in z (poling) direction is distributed through volumes 1-4.

Volume 2 consists of a passive polymer phase only and has no active phase, while the piezoelectric phases in volumes 3 and 4 are in series with the polymer in the z-direction, which results in a negligible contribution to d_{33}^{*}. Thus, only volume 1 can be considered to contribute to the effective d_{33}^{*} of the composites. The effective d_{33}^{*} of the composites can therefore be calculated by multiplying that of PZT with the fraction of load experienced by volume 1.

$$d_{33}^{*} = d_{33}^{\mathrm{PZT}}\left[1+\frac{{\rho_A}^2}{\kappa}+\frac{2\rho_A(1+\rho_A)}{1+\rho_A\kappa}\right]^{-1} \qquad (30)$$

To calculate the elastic moduli, a similar technique can also be employed to simplify the procedure.

$$Y^{*}=Y^{\mathrm{PZT}}\frac{1}{(1+\rho_A)^2}\left[1+\frac{{\rho_A}^2}{\kappa}+\frac{2\rho_A(1+\rho_A)}{1+\rho_A\kappa}\right] \tag{31}$$

In the classical theory, the composites are modeled as a homogeneous orthotropic medium with certain effective moduli that describe the “average” material properties of the composites. To describe the macroscopically homogeneous medium, macro-stress and macro-strain are derived by averaging the stress and strain tensors over the volume of the representative volume elements. In this way, the total strain energy U stored in the composite material of volume V is:

$$U=\frac{1}{2}Y_{ij}^{*}\varepsilon_{ij}^{*}V \tag{32}$$

On the other hand, the total strain energy of the composite can also be represented as a summation of strain energies of its components, by averaging the strain of each component.

$$U=\frac{1}{2}Y_{ij}^{\mathrm{PZT}}\overline{\varepsilon_{ij}^{\mathrm{PZT}}}^{2}V^{(1)}+\frac{1}{2}Y_{ij}^{\mathrm{PDMS}}\overline{\varepsilon_{ij}^{\mathrm{PDMS}}}^{2}V^{(2)} \tag{33}$$

where Y_{ij} denotes the elastic constant and $\overline{\varepsilon_{ij}}$ is the average strain of each component.

In the case of 3-D foam composites, since $Y_{ij}^{*}\sim Y_{ij}^{\mathrm{PZT}}$, we have $U\sim\frac{1}{2}Y_{ij}^{\mathrm{PZT}}\overline{\varepsilon_{ij}^{\mathrm{PZT}}}^{2}V^{\mathrm{PZT}}$. When subjected to uniaxial compression, the LTE can be estimated by

$$\eta_{3-\mathrm{D}}\simeq\sqrt{\frac{Y^{*}}{\phi Y^{(1)}}} \tag{34}$$

According to the Banno cell structure, the volume fraction is related to the aspect ratio of the PZT skeleton:

$$\phi=\frac{1+3\rho_A}{(1+\rho_A)^3} \tag{35}$$

which means that, for the 3-D foam composites:

$$\eta_{3-\mathrm{D}} \simeq \sqrt{\frac{1+\rho_A}{1+3\rho_A}\left(1+\kappa{\rho_A}^2+\frac{2\rho_A(1+\rho_A)}{1+\rho_A/\kappa}\right)} \tag{36}$$

In the case of $\rho_A \gg 1$,

$$\eta_{3-\mathrm{D}} \to \sqrt{\frac{1}{3}} = 0.57. \tag{37}$$

Let the volume fraction $\phi = 16\%$, making $\rho_A \cong 3$ and $\kappa \ll 1$, we have $\eta_{3-\mathrm{D}} \simeq 0.6325$. Considering a PDMS buffer layer that is of $\tau = 10\%$ thickness of the sample, under total 8% compression, the effective LTE is $\eta_{3-\mathrm{D}}^{*} \approx \eta_{3-\mathrm{D}}\frac{\mathrm{Y}^{\mathrm{PDMS}}}{\tau\cdot\mathrm{Y}^{*}} = \frac{(1+\rho_\mathrm{A})^2\kappa}{\tau}\sqrt{\frac{1+\rho_\mathrm{A}}{1+3\rho_\mathrm{A}}} = 1.69\times10^{-3}$.

Note S3. Finite element modeling of the transit heat transfer in the composites

In order to have a deep insight into the influence of thermal conductivity on the pyroelectric performance the composite materials, only heat conduction is taken into account and the model excludes any other form of heat transfer such as thermal convection and radiation, or any thermal strain and expansion. Under these conditions, conduction only takes place within the boundaries of the composites by the diffusion of its internal energy. The temperature within the body, *T*, is given in units of degrees Celsius or Kelvin. Its variation in space defines the temperature gradient vector, ∇T, with units of K/m. The heat flux vector, $\boldsymbol{q}$, is defined by Fourier's Conduction Law, as the thermal conductivity, k, times the negative of the temperature gradient:

$$\boldsymbol{q} = -k\nabla T \tag{38}$$

The governing equation, which related the temperature change to the heat flux, can be written as:

$$\rho c \frac{\partial T}{\partial t} = \nabla(k \nabla T) \tag{39}$$

where ρ is the density and c is the specific heat of the materials, both of them are assumed as constant and isotropic throughout the materials. Treating the thermal conductivity k as constant, then we have

$$\frac{\partial T}{\partial t} = \alpha \nabla^2 T \tag{40}$$

where $\alpha = \frac{k}{\rho c}$ denotes the thermal diffusivity.

Other than all material properties needed for a steady thermal condition, a typical transient heat transfer scenario also requires initial conditions to describe the beginning state, and boundary conditions for later times. In our simulation, the composites are set having an initial temperature of 25 $^{\circ}$C. The boundary condition is considered as a thermal sink (35 $^{\circ}$C) that is located at the bottom of the module and its thermal conductivity is assumed to be infinite. To probe the heat transfer processes, the temperature at the bottom surface has been set equal to a fixed value. All other material properties and parameters used in the simulations are listed in ESI Table S1†.

For the NP and NW composites, due to their much smaller characteristic sizes, it is unlikely for us to construct the same comprehensive nano structure of the entire sample size in finite element modeling as the 3-D foam one. Therefore, in order to compare the rate of the heat transfer among the three composites, we homogenize the NP and NW composites and calculate their effective material constants respectively.

To determine the effective thermal diffusivity of NPs and NWs composites, we simulated the processes of the flash method in ABAQUS. A high-intensity short-duration light pulse is absorbed in the bottom of the composites, and the resulting temperature history of the rear surface is recorded numerically. The effective thermal diffusivity is determined by

$$\alpha = 0.1388 \frac{h^2}{t_{0.5}} \tag{41}$$

where h denotes the thickness of the composites, and t is the time need to reach half the maximum temperature at the other end.

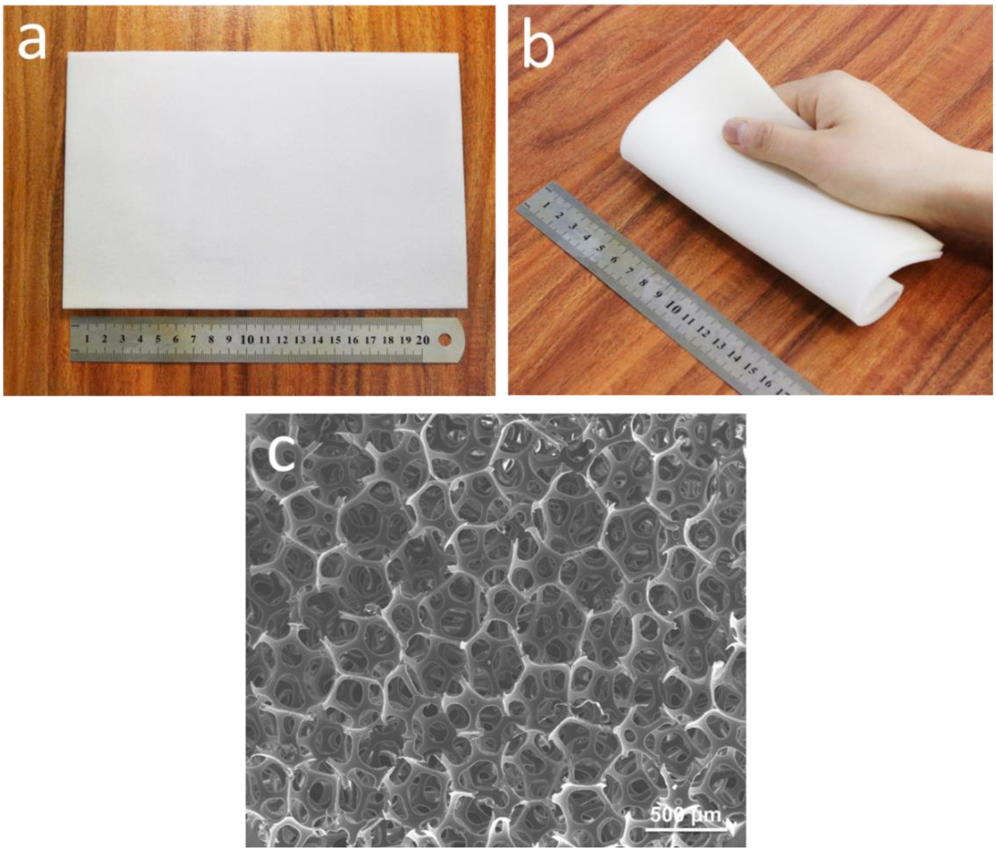

Fig. S5. (a, b) The photos of the polyurethane (PU) foam (commercially available cleanroom wiper, TX704, ITW Texwipe). (c) The SEM of the PU foam template.

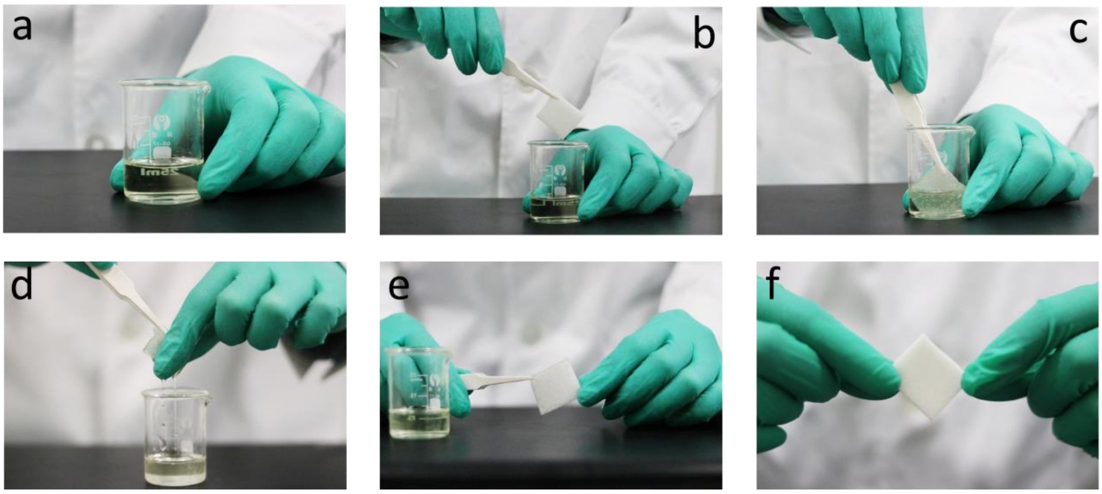

Fig. S6. The fabrication process of the 3-D foam precursor. (a) The synthesized PZT sol. (b, c) Immersing a piece of PU foam in the PZT sol. The sol is absorbed by the PU template via the capillary effect.[S7,S8] (d) Squeezing the excessive sol out from the foam. (e) The squeezed foam with an adequate amount of PZT sol. Without the squeeze process, the excessive sol fills and blocks the pores of the template, yielding an unfavorable microstructure of the PZT ceramic network with closed pores after sintering (ESI Fig. S7†). (f) The squeezed PU template with converted PZT gel after drying at 60 °C. Compared to the pristine PU foam, the weight of the template with converted PZT gel is increased 35%.

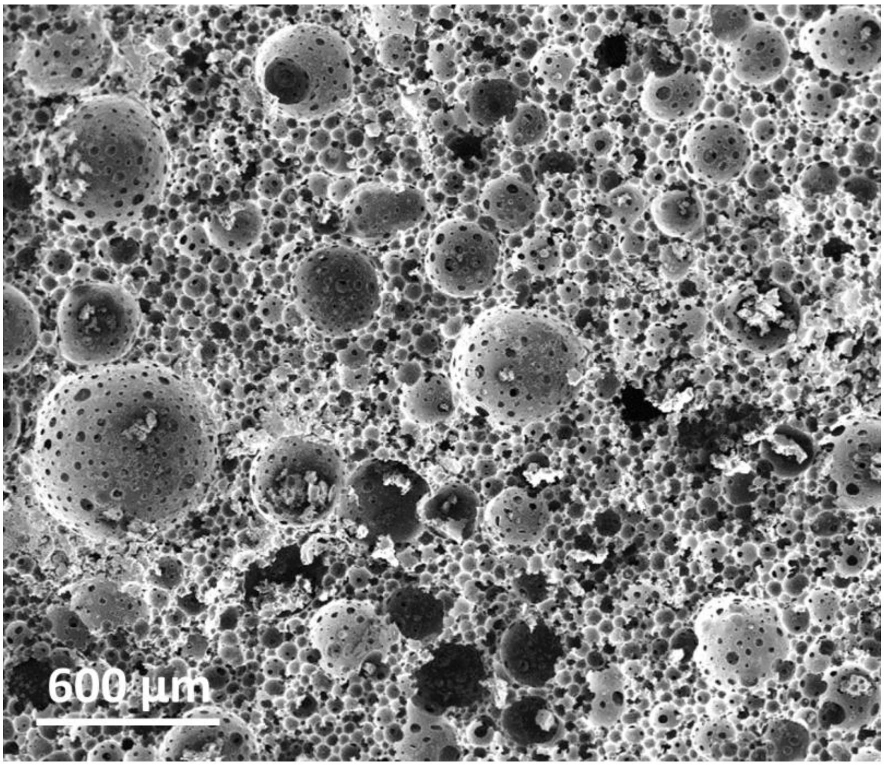

Fig. S7. SEM of the PZT ceramic foam prepared without the squeezing step. As excessive PZT sol blocks the pores of the PU template, the sintered PZT foam has closed pores with cracks.

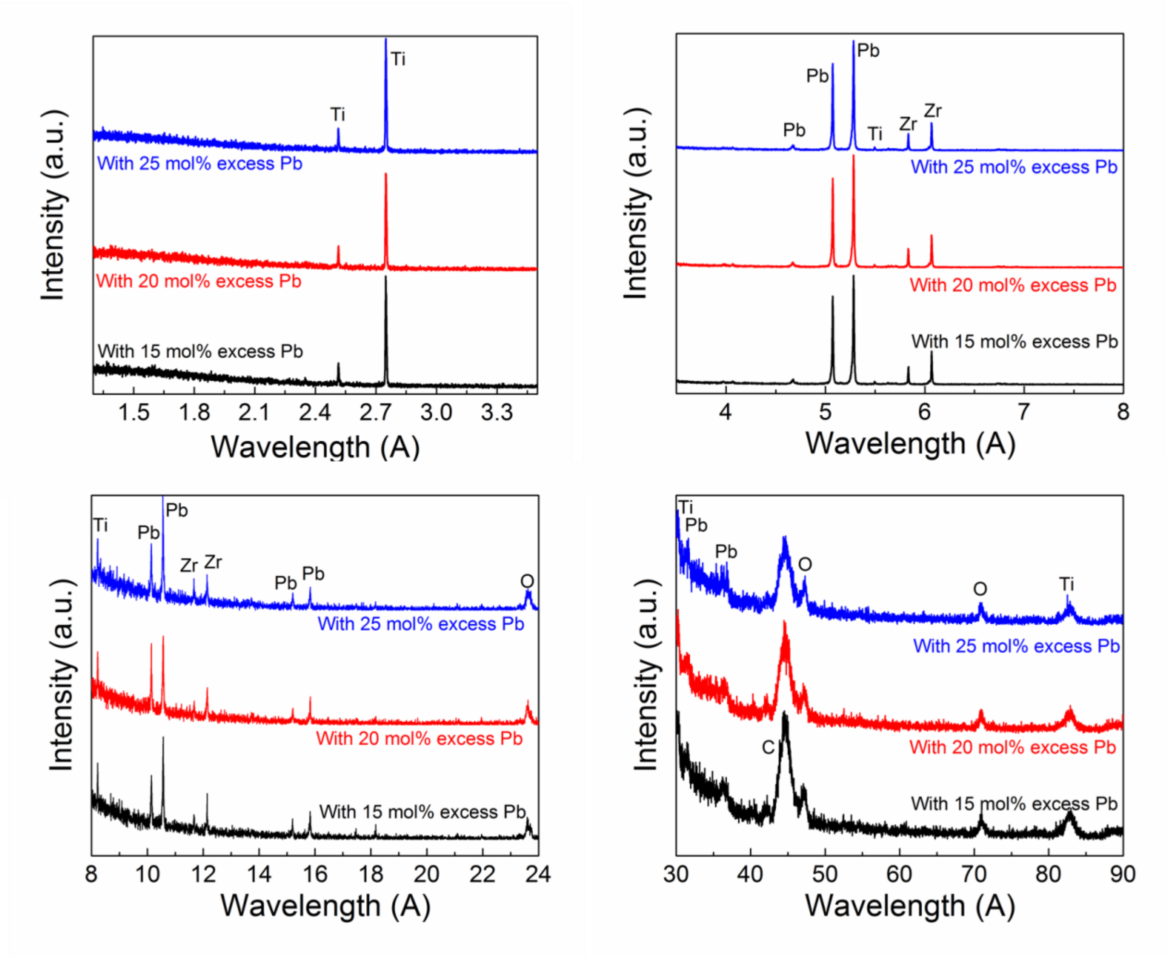

Fig. S8. EPMA profiles of the PZT 3-D ceramic microfoams prepared with various excess Pb contents. The EPMA profiles demonstrate the microfoams consist of Pb, Zr, Ti and O without impurity.

Table S2. Elemental quantitative analysis of the PZT 3-D ceramic microfoams from EPMA.

	Atomic ratio %				Atomic ratio of Pb/(Zr+Ti)	Atomic ratio of Zr/(Zr+Ti)
Excess Pb contents	Pb	Zr	Ti	O		
15 mol%	19.03	10.53	9.72	60.72	0.94	0.52
20 mol%	20.16	10.38	9.59	59.87	1.01	0.52
25 mol%	20.80	10.28	9.51	59.41	1.05	0.52

As shown in the table, Pb vacancies, e.g. atomic ratio of Pb/(Zr+Ti) < 1, exist in the PZT foams when 15 mol% excess Pb was added in the precursor. On the other hand, the loss of Pb in the heat-treatment process can be fully compensated with 20 mol% and 25 mol% excess Pb. It was found that the atomic ratio of Pb/(Zr+Ti) is very close to 1 when 20 mol% excess Pb was introduced.

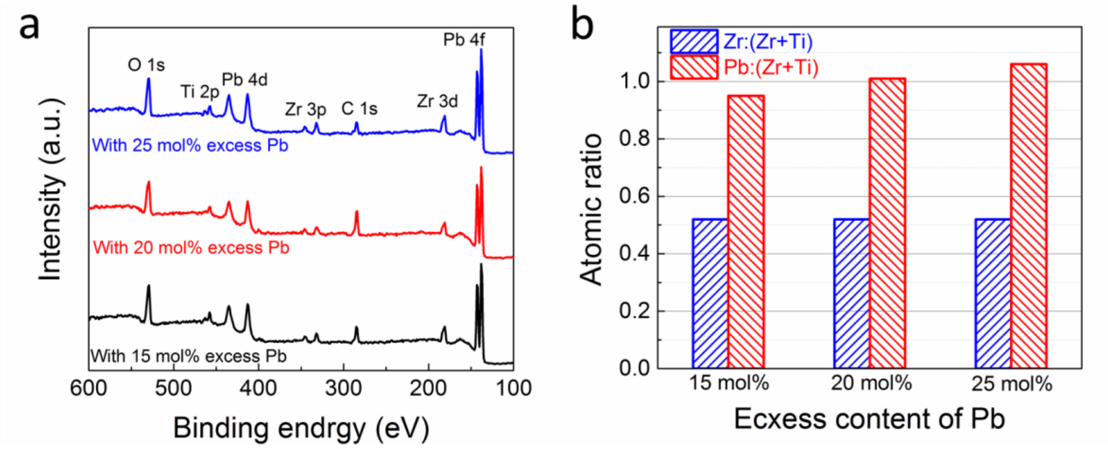

Fig. S9. (a) XPS spectra of the PZT 3-D ceramic microfoams prepared with various excess Pb contents. (b) The composition ratios of the PZT samples.

The components of the ceramic foams were calculated from the XPS patterns according to the formulas

$$X_{Zr}/(X_{Zr}+ X_{Ti})=1.004\times I_{Zr}/(I_{Zr}+1.9\times I_{Ti})-0.113 \tag{42}$$

$$X_{Pb}/(X_{Zr}+ X_{Ti})=0.152\times I_{Pb}/(I_{Zr}+1.9\times I_{Ti})+0.377 \tag{43}$$

where I_{Pb}, I_{Zr} and I_{Ti} represent XPS intensities of Pb4f, Zr3d and Ti2p peaks, respectively, and X_{Pb}, X_{Zr} and X_{Ti} are the molar ratios of Pb, Zr and Ti atoms, respectively.[S9,S10]. As shown in ESI Fig. S9b†, the Zr/Ti ratio is independent of the content of excess Pb, which is in consistent with the EPMA results. However, because of Pb volatilization during high-temperature sintering process, the content of excess Pb introduced in the precursors plays a decisive role in the final Pb content of the PZT ceramic foams. As indicated by ESI Fig. S9b†, 15 mol% excess Pb is not enough to compensate the loss of Pb during the sintering process (i.e. Pb/(Zr+Ti) ratio <1), leading to the pyrochlore phase in the sample (ESI Fig. S10†), while excessive Pb leaves in the foam (i.e. Pb/(Zr+Ti) ratio >1) with 25 mol% excess Pb. Therefore, it is suggested that 20 mol% excess Pb is an adequate content to compensate the Pb loss during the high-temperature sintering process in this work.

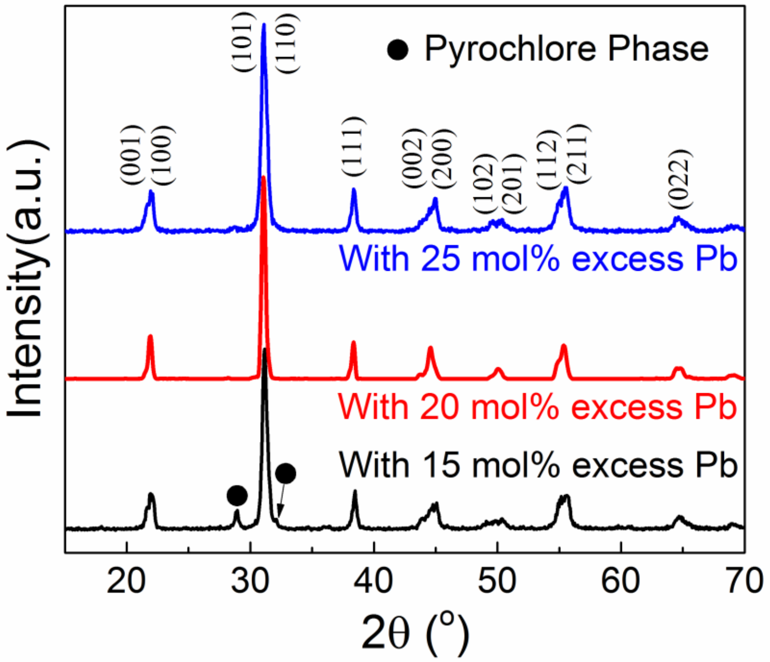

Fig. S10. XRD patterns of the PZT 3-D ceramic microfoams prepared with various excess Pb contents.

The reflections from the pyrochlore phase caused by insufficient Pb content[S11] are observed in the XRD patterns of the specimen synthesized with 15 mol% excess Pb, which is absent from the samples prepared with higher excess Pb contents (i.e. 20 mol% and 25 mol%). The XRD patterns indicate that at least 20 mol% excess Pb is required to compensate the lead volatilization during the high-temperature sintering process. The required content of excess Pb has also been confirmed by the EPMA and XPS measurements (ESI Figs. S8† and S9†, and ESI Table S2†).

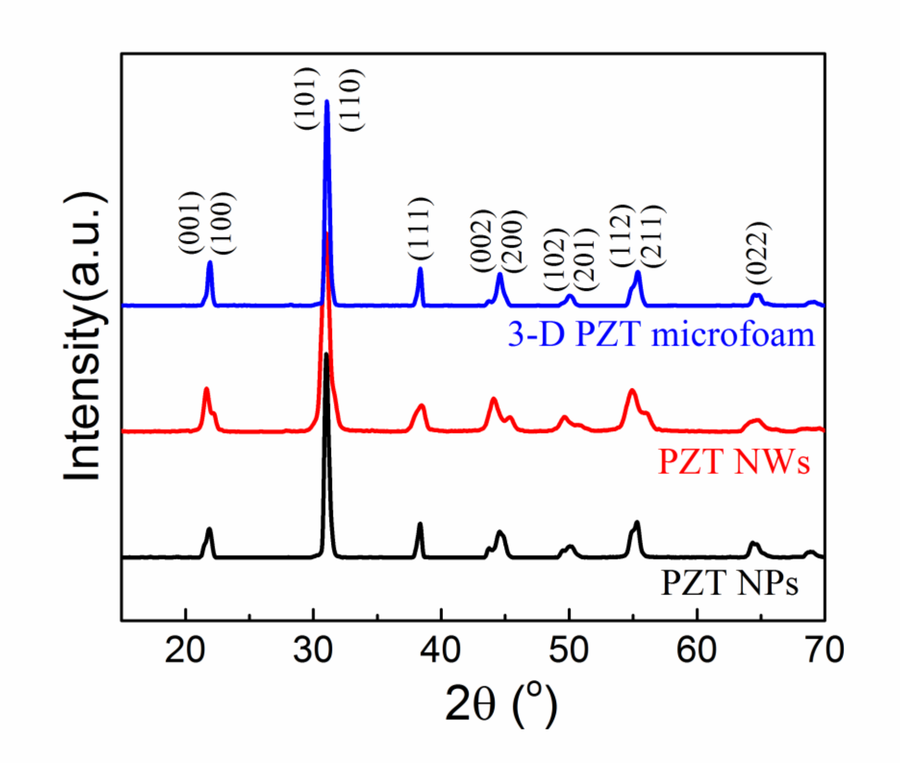

Fig. S11. XRD patterns of the PZT nanoparticles (NPs), nanowires (NWs) and 3-D ceramic microfoams.

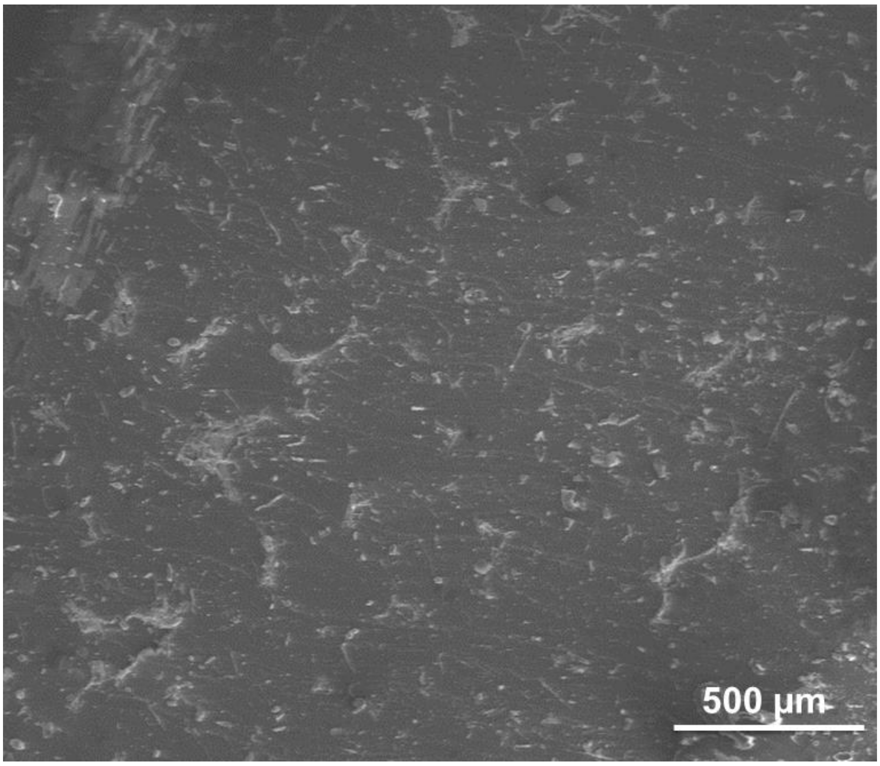

Fig. S12. The cross-section SEM of the 3-D composites.

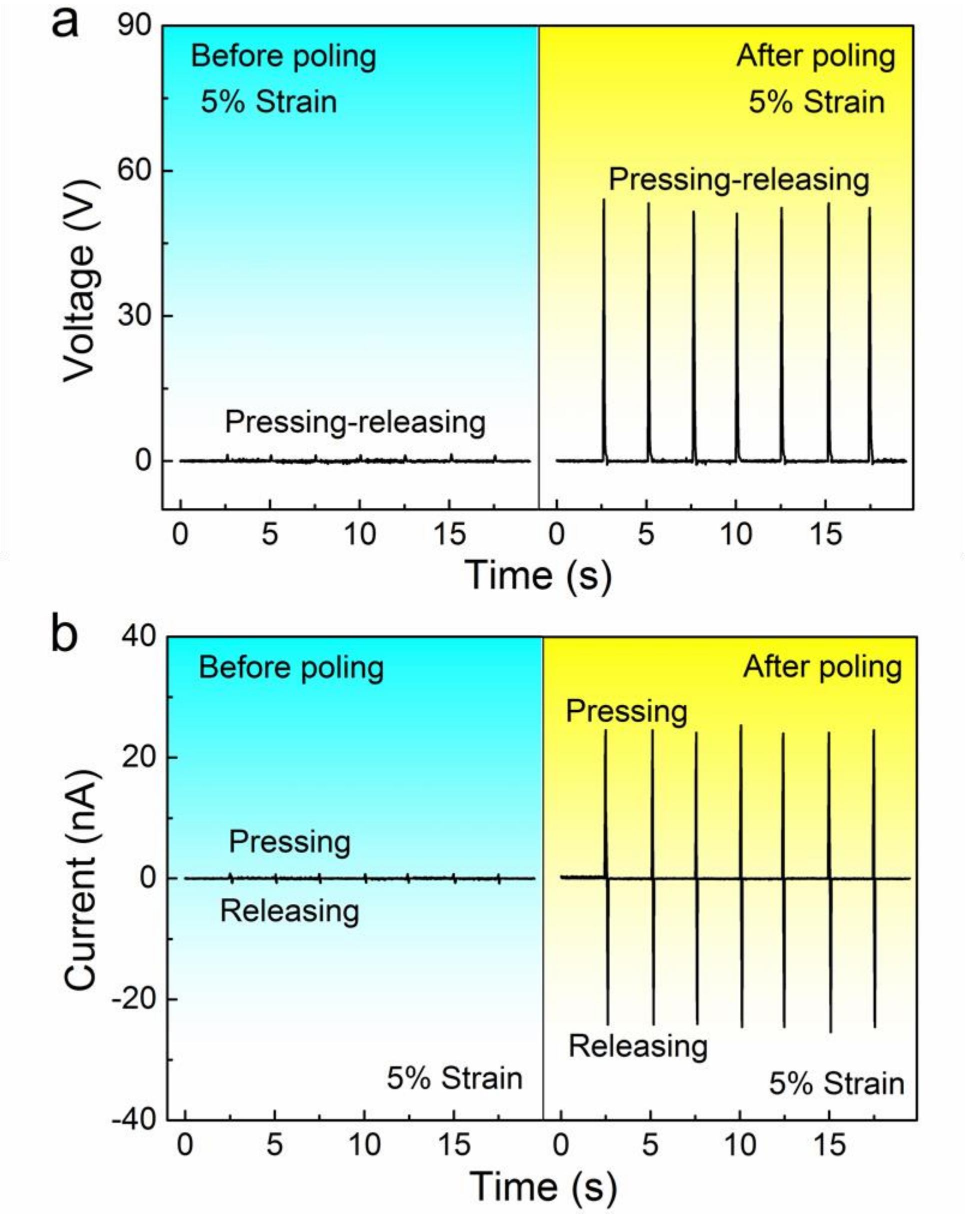

Fig. S13 The generated voltages and currents of the 3-D composites. (a) The V_{out} and (b) I_{out} signals of the 3-D composites during a periodic pressing and releasing motions (5% pressing strain) before and after poling process. Without poling, almost no piezoelectric response is observed in the sample. But after poling, significant voltage and current signals responding to the mechanical force can be achieved. The result indicates that the measured output signals are indeed piezoelectric responses which have been further confirmed by the switching-polarity tests and linear-superposition measurements (ESI Figs. S15† and S16†).

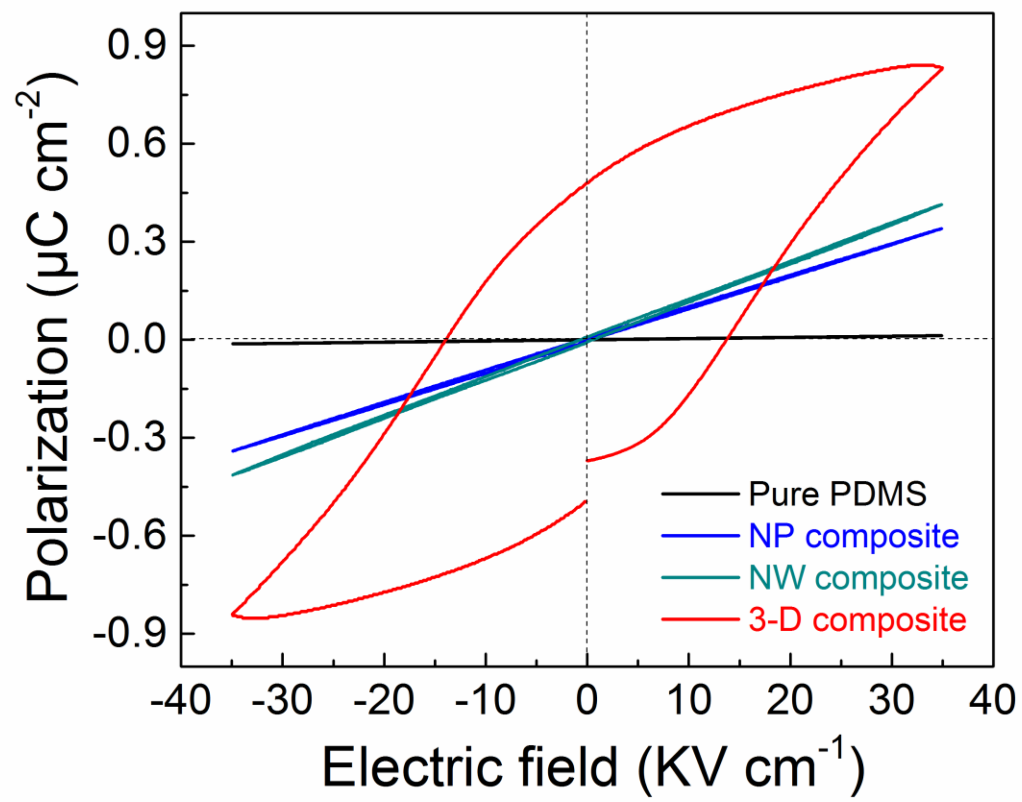

Fig. S14. The polarization-electric field (*P*-*E*) loops of PDMS and its nanocomposites measured with a frequency of 10 Hz. As a linear dielectric material, PDMS shows a low polarization of ~1.0×10^{-2} μC cm^{-2} at 35 KV cm^{-1}. The introduction of PZT leads to the increase of polarization in the composites compared to that of pure PDMS. More interestingly, with the same loading of PZT (~16 vol%), the polarization of the 3-D composite is noticeably higher than those of the low-dimensional filler based composites, which shows a ferroelectric hysteresis behavior. The high polarization and more significant ferroelectric hysteresis behavior are indicative of the favorable ferroelectric performance, including high piezoelectric and pyroelectric responses, of the 3-D interconnected composite.

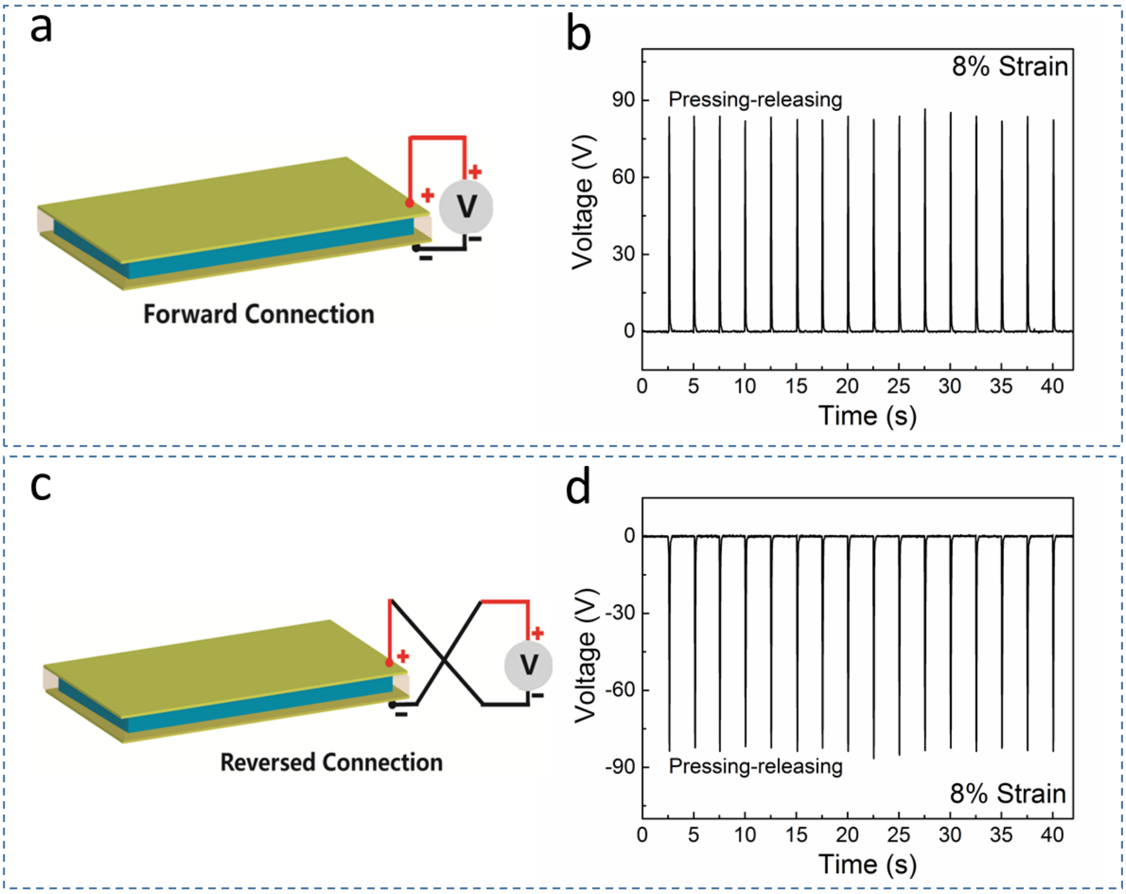

Fig. S15. The piezoelectric responses of the 3-D composites connected in different ways. (a,b) The piezoelectric signals of the 3-D composites in the forward connection during the periodic pressing and releasing motions (8% strain). (c,d) The piezoelectric responses of the 3-D composites as the samples are reversely connected. Clearly, the 3-D composites generate a positive voltage at the pressing state when it is forward connected to the measurement instruments, but negative pulses in the reverse connection.

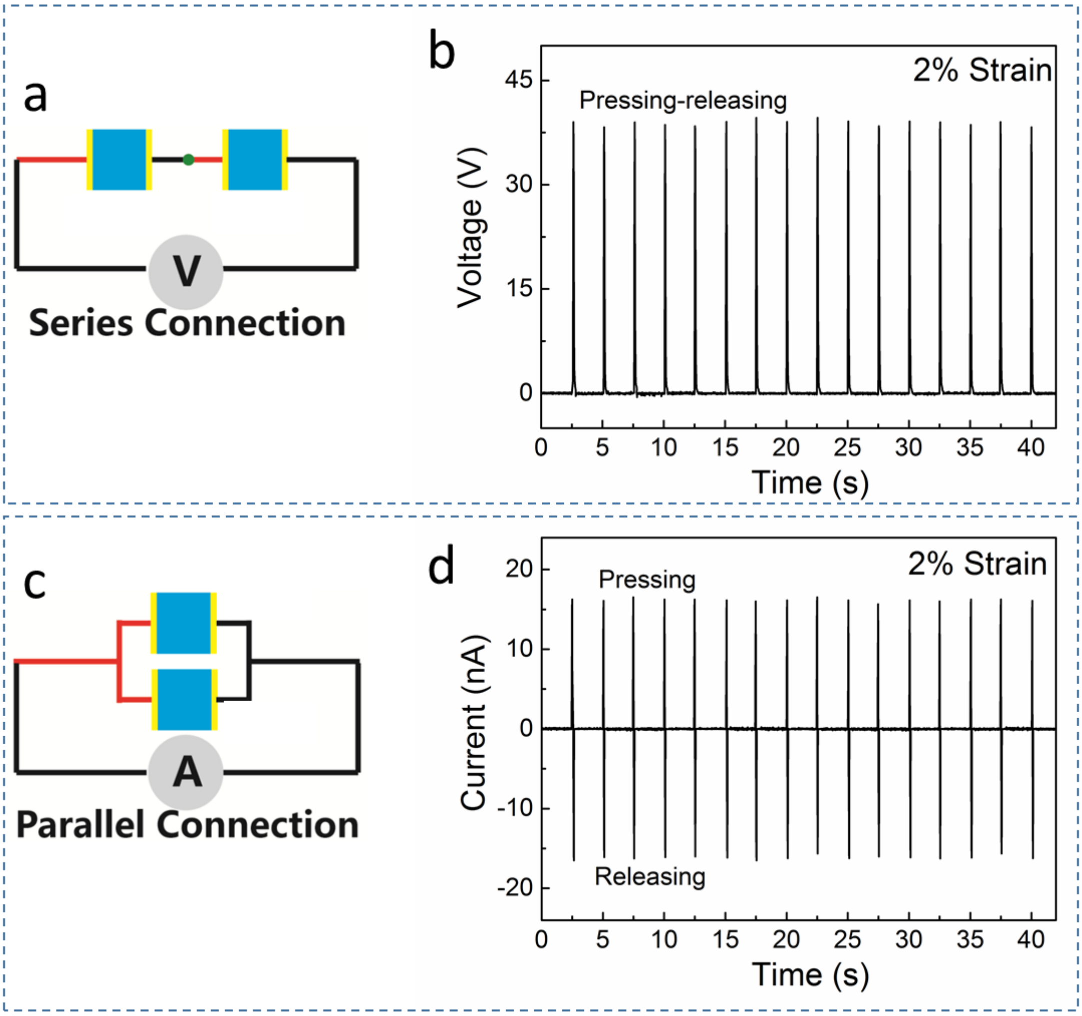

Fig. S16. The V_{out} and I_{out} of two 3-D composites connected serially and parallelly respectively under a 2% compressing strain. Both the V_{out} and I_{out} are around two times those of individual composites with the same mechanical stimulation (Fig. 2a), demonstrating again that the obtained outputs are the true signals from the piezoelectric response of the 3-D composite.

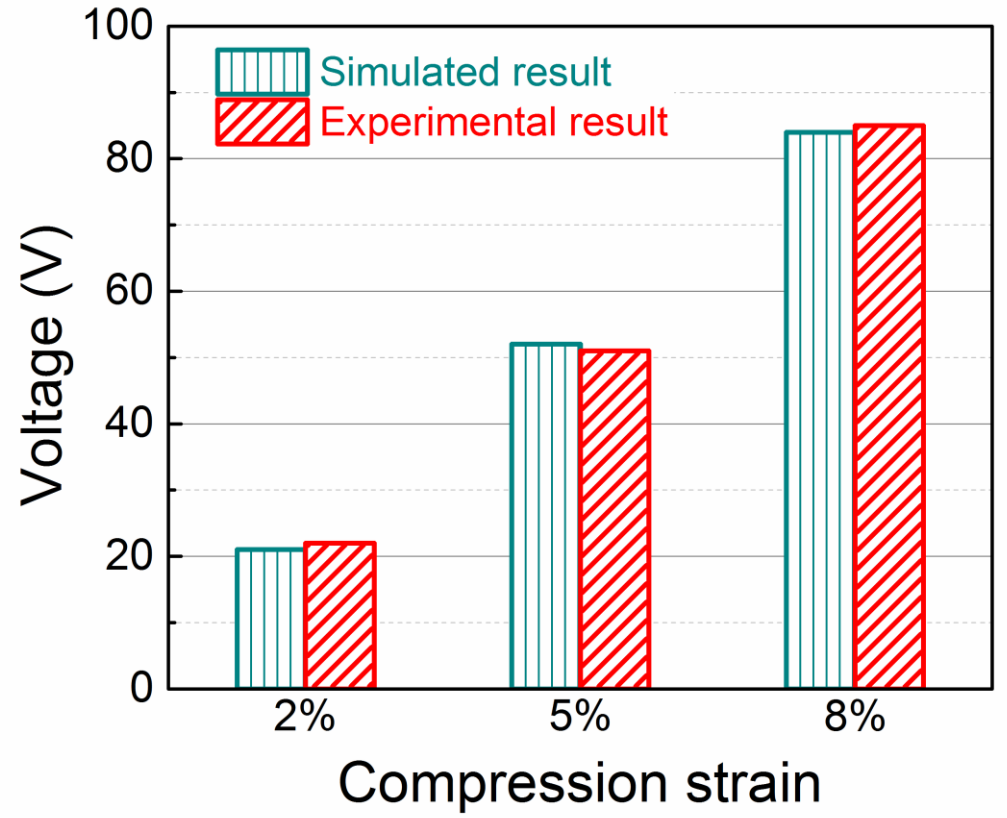

Fig. S17. The comparison of simulated and experimental piezoelectric voltages of the 3-D composites under different compressive strains. The simulated and experimental findings are in good agreement with each other.

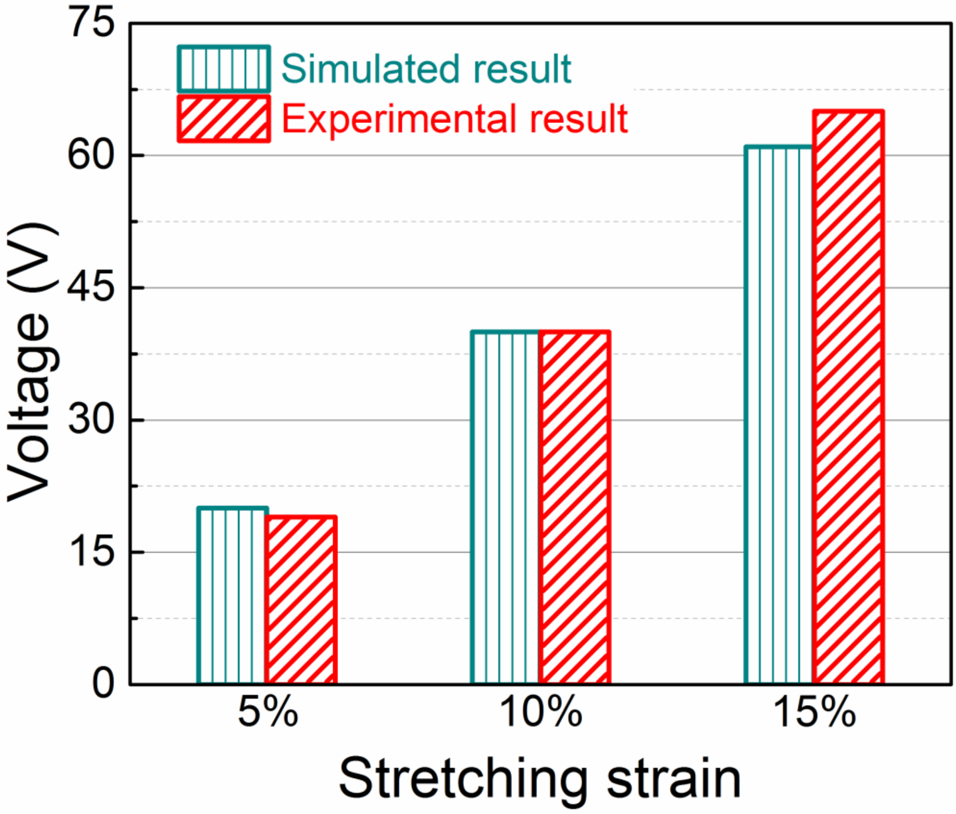

Fig. S18. The comparison of simulated and experimental piezoelectric voltages of the 3-D composites under various stretching strains. The simulated results agree with the experiments very well.

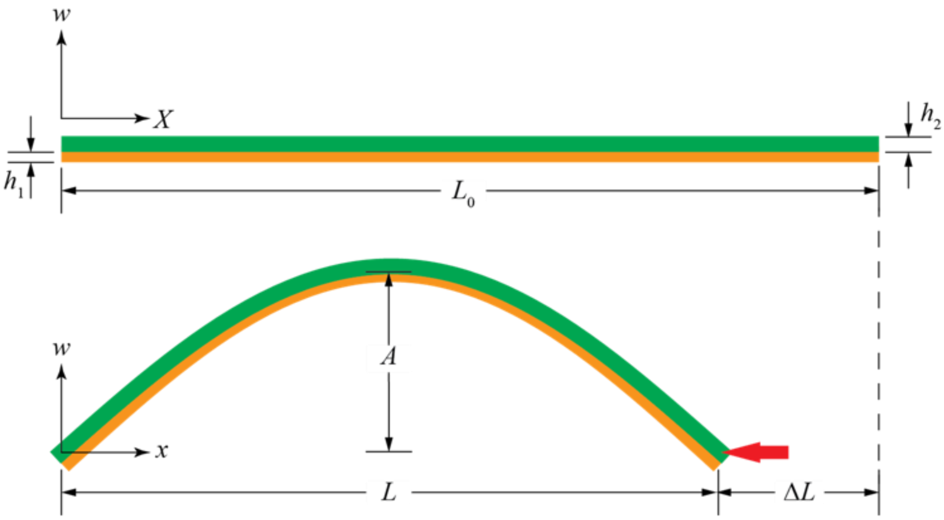

Fig. S19 Schematics of the 3-D composites under bending. The composite (green) resides on the substrate to form a thin film structure. Bending is induced by the buckling behavior of the film under a compression of ΔL between the two ends. The thicknesses of the composite (h_1) and the underlying substrate (h_2) are 1 mm and 0.4 mm, respectively.

Under compression, the out-of-plane displacement w takes the form: [S12]

$$w = A\left(\sin\frac{\pi}{L_0}X\right) \tag{44}$$

The total strain energy of the composites U^{total} consists of the bending energy U^{bending} and the membrane energy U^{membrane}. Then bending energy takes the form:

$$U^{\text{bending}} = \frac{1}{2}\int_0^{L_0}\frac{Yh^3}{12}\left(\frac{d^2w}{dX^2}\right)^2 \mathrm{d}X = \frac{Yh^3\pi^4}{48\,{L_0}^3}A^2 \tag{45}$$

where Y is Young's modulus of the membranes and h is the thickness.

The constant membrane strain ε^{m}, which determines the membrane energy, is related to the out-of-plane deflection and in-plane displacement u by

$$\varepsilon^{\text{m}} = \frac{du}{dX} + \frac{1}{2}\left(\frac{dw}{dX}\right)^2 = \text{const.} \tag{46}$$

with boundary conditions: $u(0) = 0$ and $u(L_0) = -\Delta L$, the in-plane displacement is given

$$u(X) = -\frac{\pi A^2}{8L_0}\sin\frac{2\pi X}{L_0} - \frac{\Delta L}{L}X \tag{47}$$

Hence, the membrane strain ε^{m} is:

$$\varepsilon^{\mathrm{m}} = \frac{\pi^2 A^2}{4{L_0}^2} - \frac{\Delta L}{L_0} \tag{48}$$

The membrane energy is

$$U^{\text{bending}} = \frac{YhL_0}{2}\left(\frac{\pi^2 A^2}{4{L_0}^2} - \frac{\Delta L}{L_0}\right)^2 \tag{49}$$

Minimizing U^{total} with respect to A gives the amplitude:

$$A = \frac{2L_0}{\pi}\sqrt{\frac{\Delta L}{L_0} - \frac{\pi^2}{3}\frac{h^2}{{L_0}^2}} \tag{50}$$

In the case that $\frac{\Delta L}{L_0} \gg \frac{\pi^2}{3}\frac{h^2}{{L_0}^2}$, $A \approx \frac{2}{\pi}\sqrt{L_0\Delta L}$, the strain of any point at a distance *z* above the neutral surface is expressed as: $\varepsilon_{11} = -zw''$

Therefore, the strain at the mid-plane of the composites is given by:

$$\varepsilon_{11} = \pi\frac{h_1}{L_0}\sqrt{\frac{\Delta L}{L_0}}\sin\frac{\pi X}{L_0} \tag{51}$$

where h_1 is the thickness of the substrate.

Since the piezoelectric response yields a linear relation with the strain and thickness, the piezo potential under bending test can be easily calculated by adopting the tensile experiment results. The average voltage across the composite can be written as:

$$\bar{V} = \frac{1}{L_0}\int_0^{L_0}\varepsilon_{11}\frac{V_t}{\varepsilon_t}\mathrm{d}X = \frac{2V_t}{\varepsilon_t}\frac{h_1}{L_0}\sqrt{\frac{\Delta L}{L_0}} \tag{52}$$

where V_t and ε_t denote the piezoelectric response (circuit voltage) and strain during a typical tensile test. During our stretching test, when the samples are stretched at $\varepsilon_t = 15\%$， $V_t = 62.5$ V. For the bending experiment, L_0=5 cm and h_1=0.4 mm. For ΔL=1cm and 2 cm, we have $\bar{V}$=3.0 V and 4.4 V, respectively.

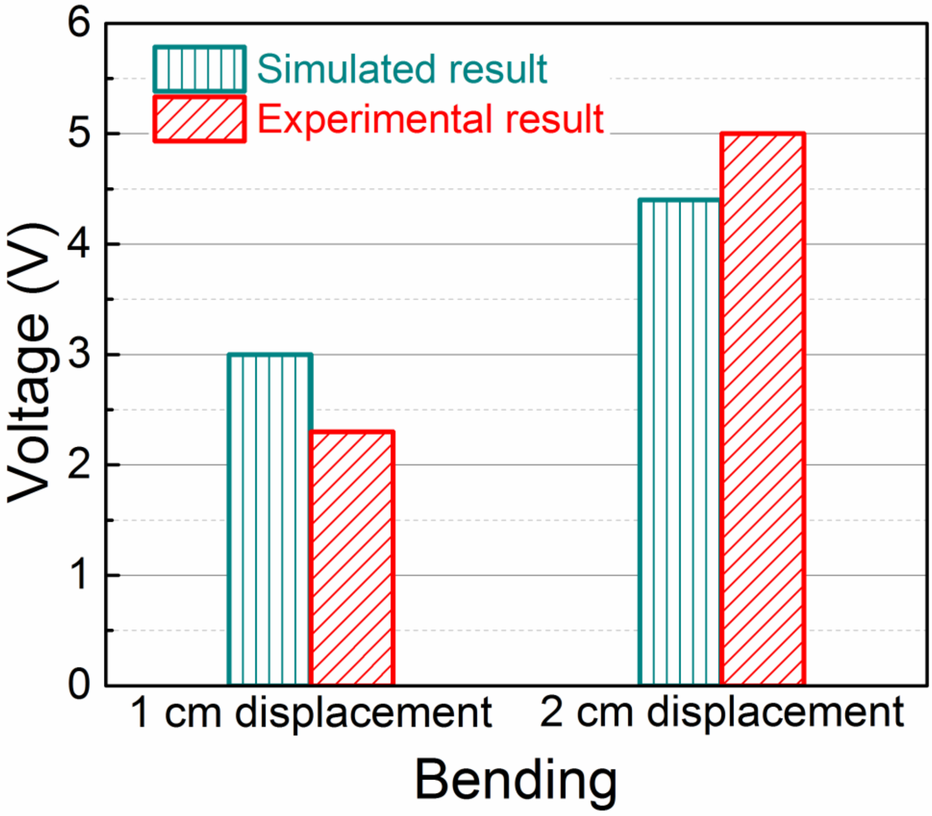

Fig. S20. The comparison of simulated and experimental piezoelectric voltages of the 3-D composites under various bending strains (a displacement of 1 cm and 2 cm from an original state of 5 cm, respectively).

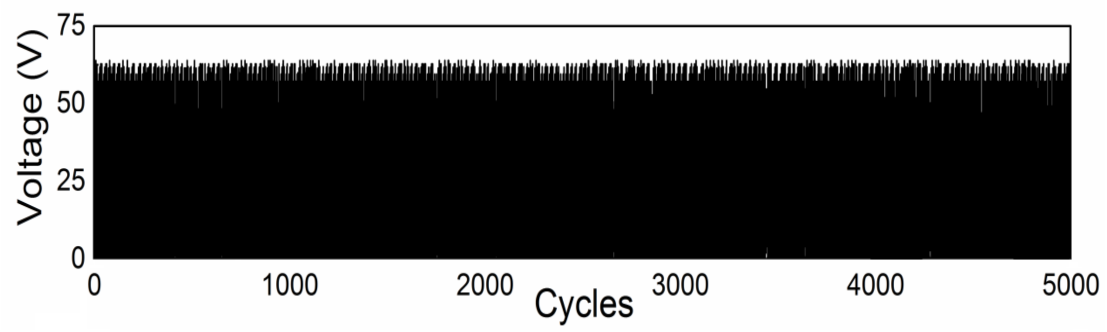

Fig. S21. The durability test result conducted to confirm the mechanical durability of the 3-D composites (stretching with 15% strain). No obvious decay in piezoelectric voltage is observed after 5000 cycles stretching.

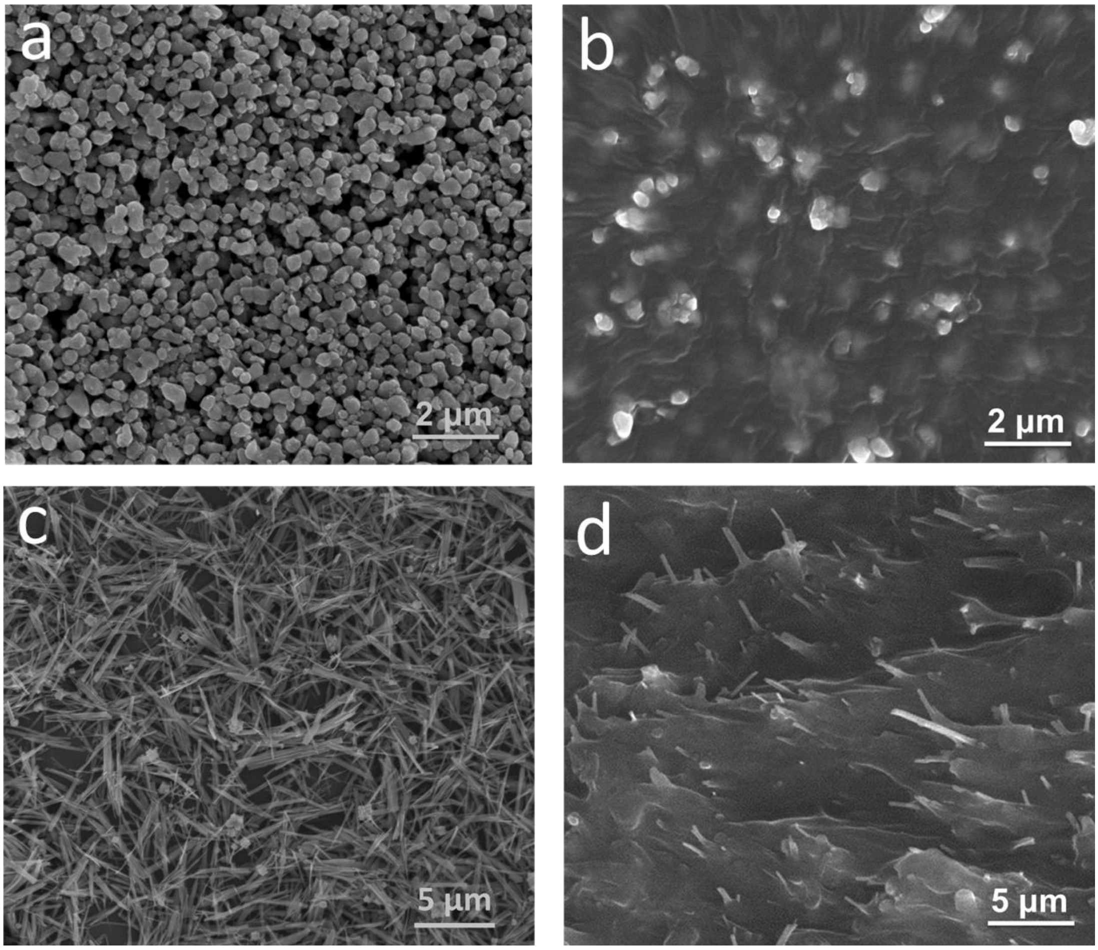

Fig. S22. SEM of the PZT NPs and NWs, and their corresponding composites. (a) The PZT NPs. (b) The NP composite. (c) The PZT NWs. (d) The NW composite.

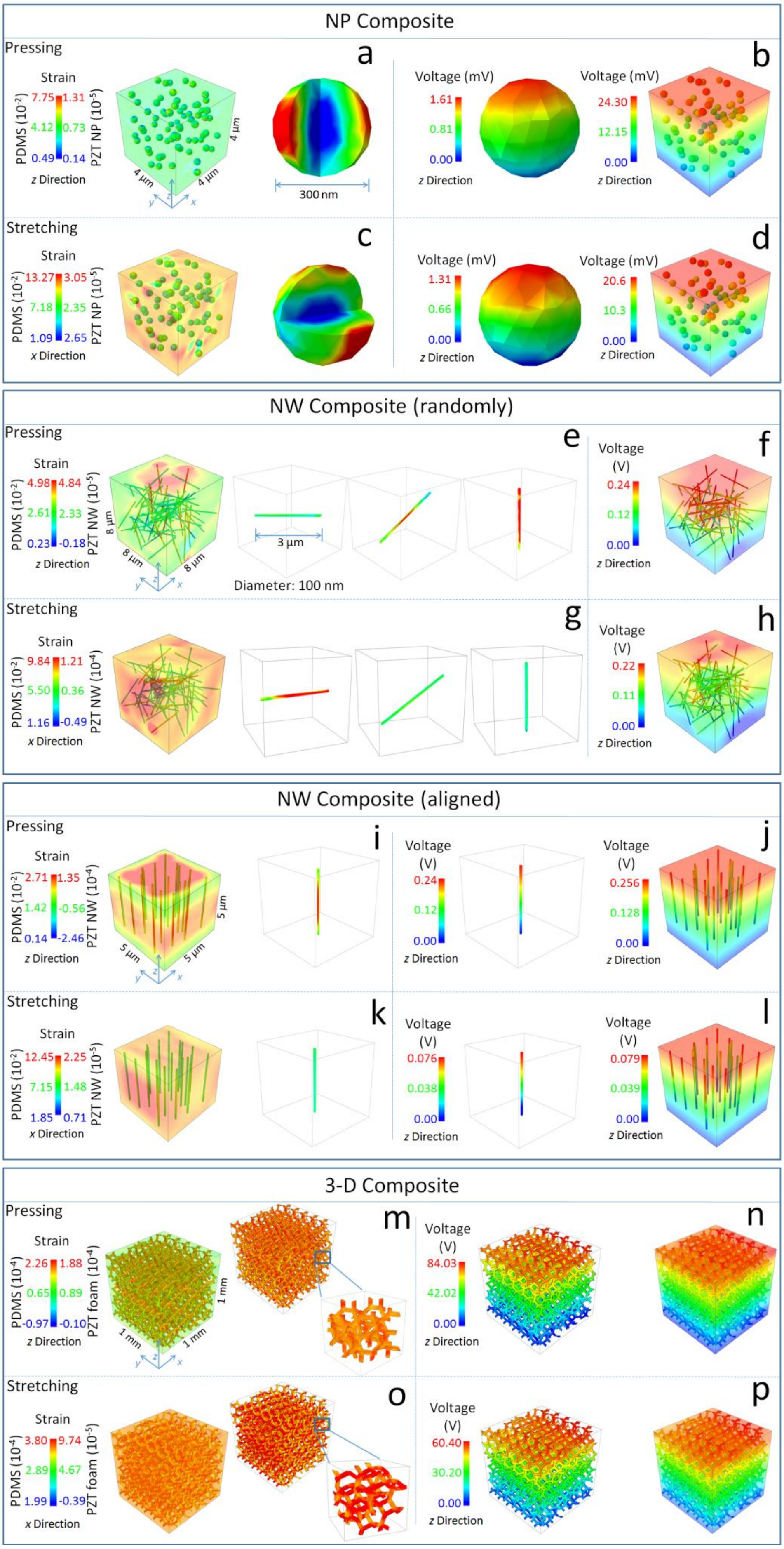
NP Composite
Pressing
a
Strain
PDMS (10⁻²)
7.75
4.12
0.49
PZT NP (10⁻⁵)
1.31
0.73
0.14
z Direction
4 μm
4 μm
4 μm
300 nm
b
Voltage (mV)
1.61
0.81
0.00
z Direction
Voltage (mV)
24.30
12.15
0.00
z Direction
Stretching
c
Strain
PDMS (10⁻²)
13.27
7.18
1.09
PZT NP (10⁻⁵)
3.05
2.35
2.65
x Direction
d
Voltage (mV)
1.31
0.66
0.00
z Direction
Voltage (mV)
20.6
10.3
0.00
z Direction
NW Composite (randomly)
Pressing
e
Strain
PDMS (10⁻²)
4.98
2.61
0.23
PZT NW (10⁻⁵)
4.84
2.33
-0.18
z Direction
8 μm
8 μm
8 μm
3 μm
Diameter: 100 nm
f
Voltage (V)
0.24
0.12
0.00
z Direction
Stretching
g
Strain
PDMS (10⁻²)
9.84
5.50
1.16
PZT NW (10⁻⁴)
1.21
0.36
-0.49
x Direction
h
Voltage (V)
0.22
0.11
0.00
z Direction
NW Composite (aligned)
Pressing
i
Strain
PDMS (10⁻²)
2.71
1.42
0.14
PZT NW (10⁻⁴)
1.35
-0.56
-2.46
z Direction
5 μm
5 μm
5 μm
Voltage (V)
0.24
0.12
0.00
z Direction
j
Voltage (V)
0.256
0.128
0.00
z Direction
Stretching
k
Strain
PDMS (10⁻²)
12.45
7.15
1.85
PZT NW (10⁻⁵)
2.25
1.48
0.71
x Direction
Voltage (V)
0.076
0.038
0.00
z Direction
l
Voltage (V)
0.079
0.039
0.00
z Direction
3-D Composite
Pressing
m
Strain
PDMS (10⁻⁴)
2.26
0.65
-0.97
PZT foam (10⁻⁴)
1.88
0.89
-0.10
z Direction
1 mm
1 mm
1 mm
n
Voltage (V)
84.03
42.02
0.00
z Direction
Stretching
o
Strain
PDMS (10⁻⁴)
3.80
2.89
1.99
PZT foam (10⁻⁵)
9.74
4.67
-0.39
x Direction
p
Voltage (V)
60.40
30.20
0.00
z Direction

Fig. S23. Simulation of the strain and voltage distributions of the NP, NW and 3-D composites under 8% compression and 15% stretching. (a) Strains on a NP composite cell and a dissected PZT NP when the composites are subjected to 8% pressing strain. (b) The compressive strain induced piezoelectric voltages on the PZT NP and the composite cell. (c) Strains on a NP composite cell and a dissected PZT NP when the composites are stretched with 15% strain. (d) The stretching induced piezoelectric voltages on the PZT NP and the composite cell. (e) Strain on the NW composite cell with randomly orientated NWs. The local strains on the NWs depend on their orientations (8% compression is applied on the whole composite). (f) The compressive strain stimulated piezoelectric voltage on the composite cell. (g) Strain on the NW composite cell with randomly orientated NWs. The local strain on the NWs is determined by their orientation as well (15% stretching is applied on the whole composite). (h) The stretching strain stimulated piezoelectric voltage on the composite cell. (i) Strain on the NW composite cell with NWs orientated along the compressive direction when 8% pressing is applied on the whole composite. The local strain on a NW is also presented. (j) Pressing generated piezoelectric voltages on a NW and the composite cell. (k) Strain on the aligned-NW composite cell and a single NW when the whole composite is subjected to 15% stretching. (l) Stretching generated piezoelectric voltages of a NW and the composite cell. (m) Strains on a 3-D composite and the PZT skeleton when the composite is subjected to 8% pressing strain. (n) The compressive strain induced piezoelectric voltage on the PZT foam and the composite. (o) Strains on a 3-D composite and the PZT skeleton when the composite is stretched with 15% strain. (p) The stretching induced piezoelectric voltage on the PZT foam and the composite.

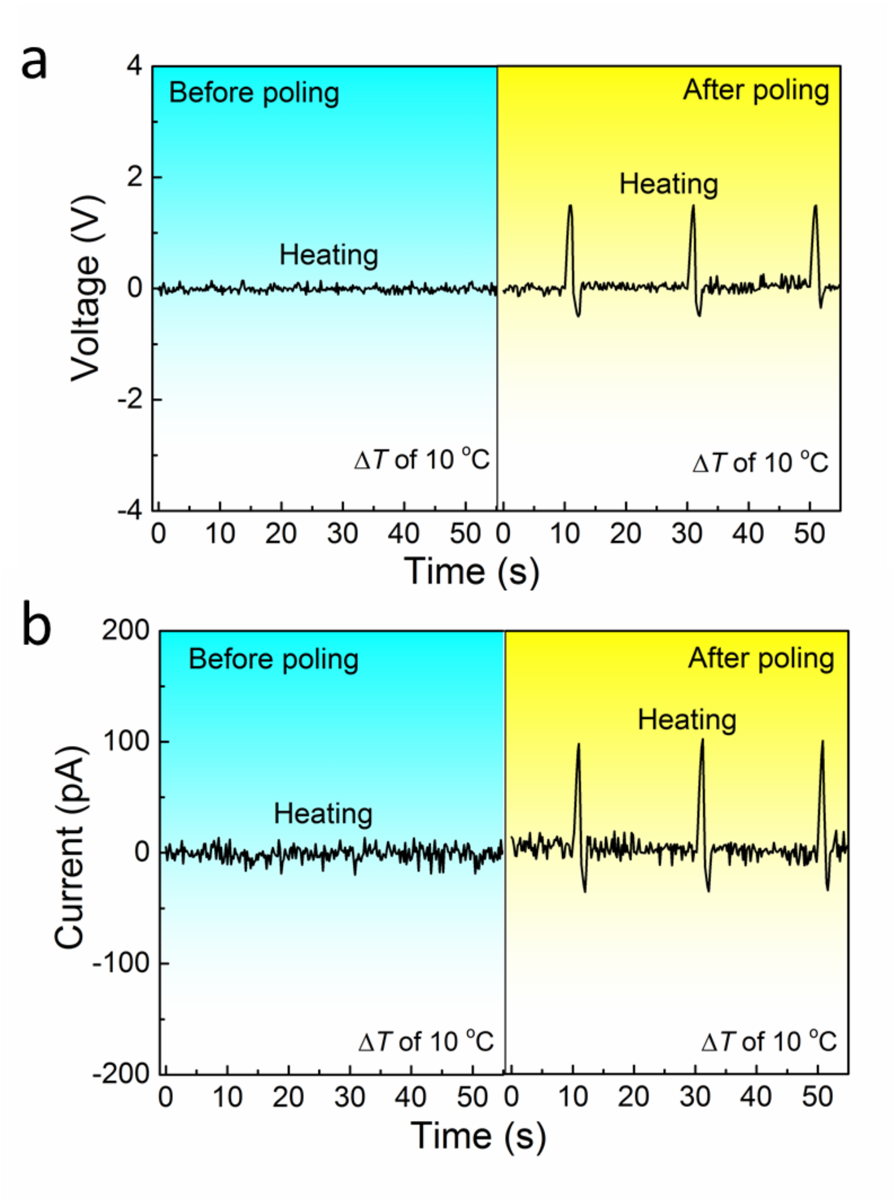

Fig. S24. The V_{out} and I_{out} signals of the 3-D composites under the heat condition (ΔT of 10 ^{o}C) before and after poling process.

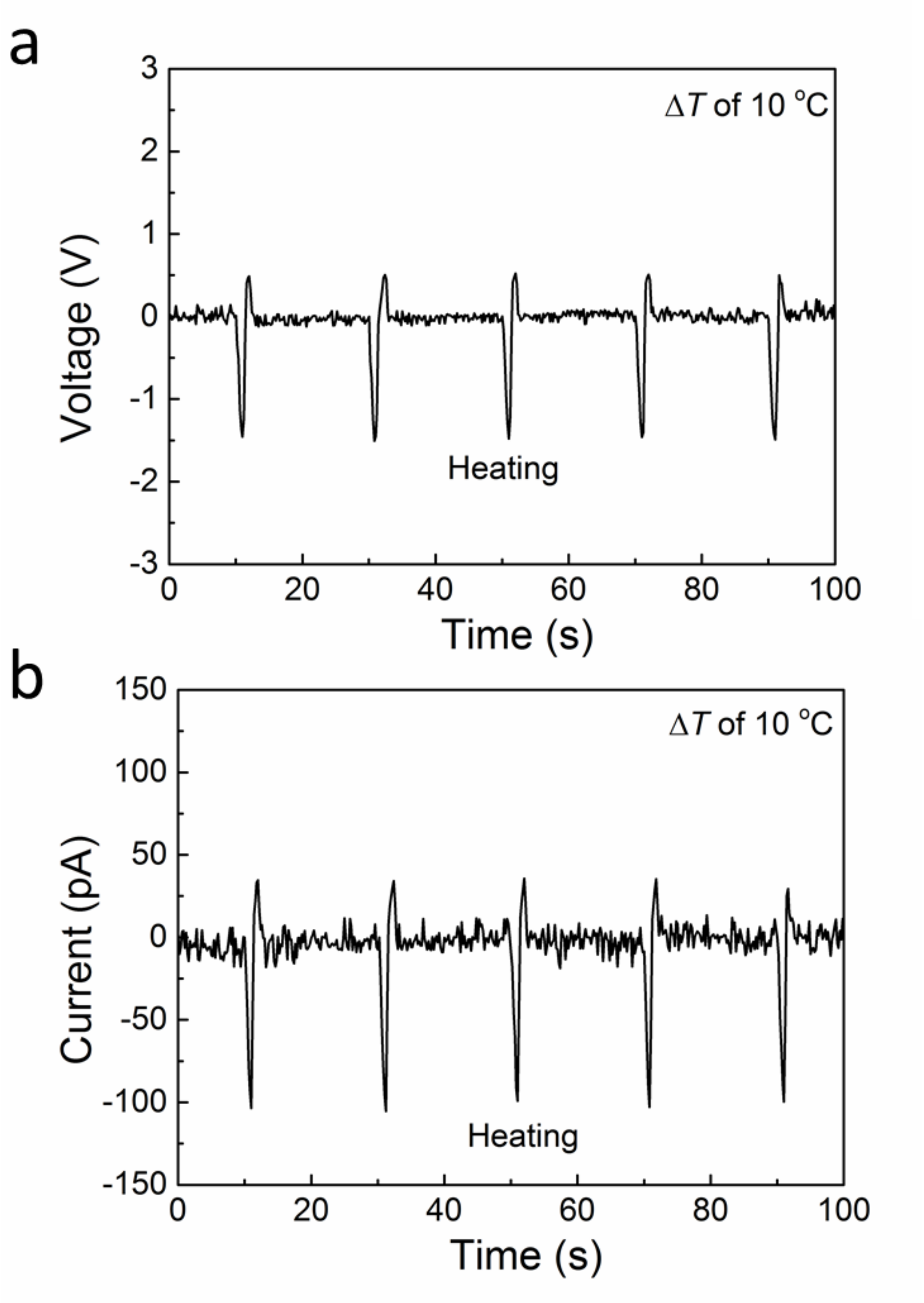

Fig. S25. V_{out} and I_{out} signals of the 3-D composites in the reversed connection under the heat condition (ΔT of 10 ^{o}C).

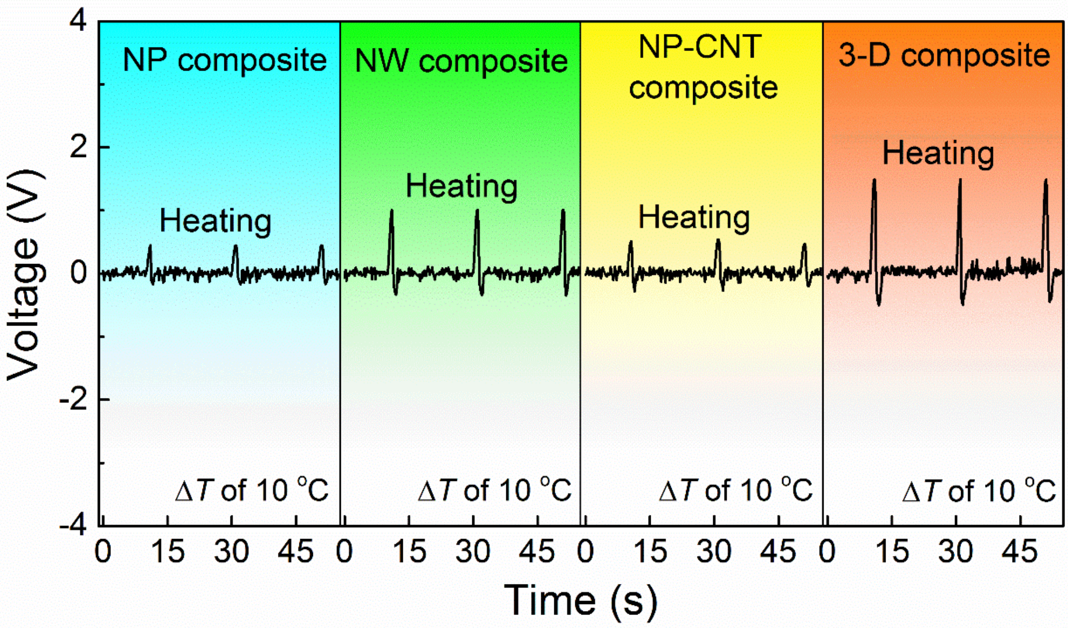

Fig. S26. Pyroelectric output voltages of the NP, NW, NP-CNT and 3-D composites under a temperature fluctuation of 10 °C.

Table S3. Simulated and tested piezoelectric voltages of the composites under compression, stretching and bending.

	Pressing with 8% strain		Stretching with 15% strain		Bending with 2 cm displacement	
	Simulated voltage (V)	Experimental voltage (V)	Simulated voltage (V)	Experimental voltage (V)	Simulated voltage (V)	Experimental voltage (V)
NP composite	6	7	5	5	0.34	0.5
NW composite (random)	32	37	26	30	2.02	2.3
NW composite (aligned)	47	--	14	--	0.94	--
NP-CNT composite	--	27	--	20	--	1.3
3-D composite	84	85	61	65	4.39	5.0

Supplementary References

S1 Abaqus analysis user's manual v.6.10. Dassault Systèmes Simulia Corp., Providence, RI.

S2 T. Furukawa, K. Fujino and E. Fukada, *Jpn. J. Appl. Phys.*, 1976, **15,** 2119.

S3 L. Sun and K. Keshoju, *Mater. Res. Soc. Symp. Proc.*, 2008, **1058,** JJ06.

S4 J. C. H. Affdl and J. L. Kardos, *Polym. Eng. Sci.*, 1976, **16**, 344.

S5 K. Rittenmyer, T. Shrout, W. A. Schulze and R. E. Newnham, *Ferroelectrics*, 1982, **41,** 189.

S6 C. R. Bowen, A. Perry, H. Kara, and S. W. Mahon, *J. Eur. Ceram. Soc.*, 2001, **21,** 1463.

S7 S. Kobayashi and B. Zeegers, *J. Cell. Plast.*, 1988, **24,** 80.

S8 J. Ha, J. Kim, Y. Jung, G. Yun, D.-N. Kim and H.-Y. Kim, *Sci. Adv.*, 2018, **4**, eaao7051.

S9 O. Sugiyama and K. Murakami, S. Kaneko, *J. Eur. Ceram. Soc.*, 2004, **24,** 1157.

S10 O. Sugiyama, S. Saito, K. Kato, S. Osumi and S. Kaneko, *Jpn. J. Appl. Phys.*, 1999, **38**, 5461.

S11 C. D. E. Lakeman and D. A. Payne, *J. Am. Ceram. Soc.*, 1992, **75**, 3091.

S12 J. Song, Y. Huang, J. Xiao, S. Wang, K. C. Hwang, H. C. Ko, D.-H. Kim, M. P. Stoykovich and J. A. Rogers, *J. Appl. Phys.*, 2009, **105,** 123516.